coatings

MDPI

Article

Numerical Simulation of Ice Crystal Accretion and Aerodynamic Impacts on Wind Turbine Blades in Cold Climates

Bo Yang [1], Afang Jin [1,*], Jing Cheng [2], Shuhao Zhou [1] and Bang Jiang [3]

[1] College of Mechanical Engineering, Xinjiang University, Urumqi 830047, China; boyang@stu.xju.edu.cn (B.Y.)
[2] School of Electrical Engineering, Xinjiang University, Urumqi 830047, China
[3] Wind Power Products Division, Zhu Zhou Times New Material Technology Co., Ltd., Zhuzhou 412000, China
* Correspondence: efang3500@sina.com

Abstract: With the advancement of science and technology, wind power generation has been widely adopted globally. However, ice accretion severely limits the operational efficiency and structural safety of wind turbines in cold regions, while existing research primarily focuses on the impact of supercooled droplets on blade icing, the influence of ice crystals in cold environments on the blade icing process has been largely overlooked. This study systematically simulated the accretion of ice crystals and supercooled droplets under clear ice conditions. It evaluated the effects of various ice crystal parameters on the icing process using Fensap-Ice, which is an advanced icing simulation tool. The results indicate that ice accretion, driven by the combined action of ice crystals and supercooled droplets, weakened ice corners, making the ice shape smoother and fuller. When the angle of attack of the ice-covered airfoil exceeded 15°, a separating vortex formed on the suction side of the blade, leading to a reduction in the lift coefficient. The findings of this study highlight the critical role of ice crystals in the icing process and provide a scientific foundation for understanding the icing mechanism under complex meteorological conditions.

Keywords: wind turbine icing; numerical simulations; ice crystal; aerodynamic impacts

check for updates

Received: 18 December 2024
Revised: 14 January 2025
Accepted: 20 January 2025
Published: 22 January 2025

Citation: Yang, B.; Jin, A.; Cheng, J.; Zhou, S.; Jiang, B. Numerical Simulation of Ice Crystal Accretion and Aerodynamic Impacts on Wind Turbine Blades in Cold Climates. *Coatings* **2025**, *15*, 126. https://doi.org/10.3390/coatings15020126

Copyright: © 2025 by the authors. Licensee MDPI, Basel, Switzerland. This article is an open access article distributed under the terms and conditions of the Creative Commons Attribution (CC BY) license (https://creativecommons.org/licenses/by/4.0/).

1. Introduction

Wind power, as a clean and renewable energy source, has been widely adopted globally. However, wind turbines typically operate in wet, cold, mountainous environments. Despite the abundant wind resources in these regions, ice accretion on the blade surface significantly impacts the operational efficiency and structural safety of wind turbine units [1,2], becoming a critical factor limiting the development of wind power technology in cold regions [3].

This ice accretion poses a serious threat to the safe operation of wind turbines [4]. Ice accumulation increases the blade surface's roughness and weakens aerodynamic performance, leading to reduced lift and increased drag [5]. This directly affects the turbine's energy capture efficiency and may lead to load imbalances, increasing stress on bearings and the transmission system [6]. When the ice mass reaches a certain level, it can trigger blade resonance and vibration fatigue [7]. In extreme cases, it can cause turbine collapse [8].

With the ongoing global development of wind energy technologies, significant progress has been made in ice accretion research, particularly regarding the mechanisms of ice formation, the aerodynamic performance of iced blades, and the development of de-icing and anti-icing technologies [9–11]. For example, Homola et al., through wind tunnel experiments, found that temperatures and relative humidity directly affect the rate and thickness of ice formation on the blade surface [12]. Their results indicate that under low temperature and high humidity, the speed of ice accretion increases and the ice layer

thickens significantly, reducing the aerodynamic performance of the blades. Wang studied the effect of wind speed on the ice accretion process using numerical simulations [13]. The results showed that as wind speed increases, the frequency and kinetic energy of droplet impacts on the blade surface also increase, leading to broader ice coverage on the windward side. Timmer et al. demonstrated through experiments that the angle of attack (AOA) influences the ice shape, with larger AoA at higher rotational speeds leading to more severe icing [14]. Ozcan Yirtici et al. utilized the Blade Element Momentum (BEM) method combined with an ice accretion prediction approach based on the Extended Messenger model to investigate the impact of ice accretion on the aerodynamic performance of wind turbine blades, finding a significant power loss of approximately 20% [15]. Linyue Gao et al. conducted experiments in an icing wind tunnel to analyze the aerodynamic performance degradation of wind turbine blades under typical glaze ice conditions, concluding that at low angles of attack, lift significantly decreases to 12% of its original value, while drag increases by 4.5 times [16]. Additionally, Guan et al. conducted a numerical simulation showing that the thickness and distribution of the ice layer directly affect the lift and drag characteristics of the blades, reducing turbine output power [17]. Sokolov et al. also analyzed the effect of blade rotational speed on the icing process. They found that higher speeds increase centrifugal forces, affecting ice formation and distribution and altering the aerodynamic properties of the blades [18].

Existing research has thoroughly examined blade icing caused by supercooled droplets and has made significant progress [19–21]. Nevertheless, significant gaps remain regarding the accretion of ice crystals, particularly their influence on the blade icing process and the aerodynamic performance of iced blades. In cold regions, ice crystals and supercooled droplets typically coexist in the atmosphere. Ice crystals are formed through the direct condensation of atmospheric water vapor or by freezing liquid droplets. The diameter, concentration, and aspect ratio of ice crystals significantly influence their settling velocity and spatial distribution in the atmosphere. In extreme weather conditions, such as blizzards or windblown snow, the atmosphere contains large quantities of ice crystals, further complicating and increasing the uncertainty of blade icing.

This paper aims to reveal the mechanism of ice accretion on wind turbines under the coexistence of ice crystals and supercooled droplets by analyzing the icing process of the turbines under complex meteorological conditions. By investigating the interaction between ice crystals and droplets during ice accretion, we explored the characteristics of the ice shape and thoroughly examined the impact of ice crystals on the aerodynamic performance of the airfoil. This research not only broadens the understanding of the icing process under complex weather conditions but also provides essential theoretical support for optimizing wind turbine blade design and anti-icing technologies.

2. Numerical Method

2.1. Simulation Process

Numerical modeling techniques have become a critical research method for studying ice accretion phenomena. In particular, for ice accretion behavior under complex meteorological conditions, numerical simulations provide accurate and efficient predictions of the ice shape. FENSAP-ICE [22–24], one of the most established ice accretion simulation tools, has been widely recognized and utilized by researchers for its excellent simulation capabilities. In this study, FENSAP-ICE was employed to predict the ice shape on the blade surface of a wind turbine, exploring the ice accretion process and the aerodynamic characteristics of the blade surface under complex meteorological conditions. The numerical simulation calculation process for this study is shown in Figure 1.

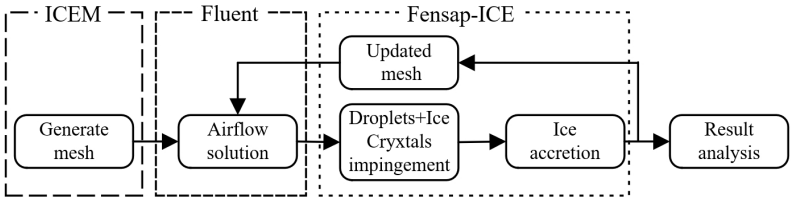

Figure 1. Numerical simulation calculation process.

2.2. Airflow Solution

The airflow solution is obtained using Fluent 2020R1 software. To address the aerodynamic problem, the Fluent solver employs a continuity equation, a momentum equation, and an energy equation. The governing equations are presented in Equations (1)–(3) [25].

The continuity equation is as follows:

$$\frac{\partial \rho_a}{\partial t} + \vec{\nabla} \cdot (\rho_a \vec{V}_a) = 0 \tag{1}$$

where t is time, $\vec{V}_a$ is the airflow velocity, and ρ_a is air density.

The momentum equation is as follows:

$$\frac{\partial \rho_a \vec{V}_a}{\partial t} + \vec{\nabla} \cdot (\rho_a \vec{V}_a \vec{V}_a) = \vec{\nabla} \cdot \vec{\sigma}^{ij} + \rho_a \vec{g} \tag{2}$$

where σ^{ij} is the stress tensor component and $\vec{g}$ is the gravity vector.

The energy equation is as follows:

$$\frac{\partial \rho_a E_a}{\partial t} + \vec{\nabla} \cdot (\rho_a \vec{\nabla}_a H_a) = \vec{\nabla} \cdot \left(\kappa_a (\vec{\nabla} T_a) + v_i \vec{\tau}^{ij} \right) + \rho_a \vec{g} \cdot \vec{V}_a \tag{3}$$

where E_a is air internal energy and H_a is air internal enthalpy.

The Spalart–Allmaras model offers an efficient computational approach for the calculation of aerodynamic properties of airfoils and has become a widely used turbulence model in the analysis of aerodynamic characteristics [26]. The modeling of turbulent viscosity and the transport equation for the Spalart–Allmaras model are shown in Equations (4) and (5).

$$\mu_T = \rho \tilde{v} f_{v1} \tag{4}$$

$$\frac{\partial}{\partial t}(\rho \tilde{v}) + \frac{\partial}{\partial x_i}(\rho \tilde{v} u_i) = G_v + \frac{1}{\sigma_{\tilde{v}}} \left[\frac{\partial}{\partial x_j} \left\{ (\mu + \rho \tilde{v}) \frac{\partial \tilde{v}}{\partial x_j} \right\} + C_{b2} \rho \left(\frac{\partial \tilde{v}}{\partial x_j} \right)^2 \right] - Y_v + S_{\tilde{v}} \tag{5}$$

where ρ is density, $\tilde{v}$ is turbulent kinematic viscosity, f_{v1} is the viscous damping function, G_v is the production of turbulent viscosity, Y_v is the destruction of turbulent viscosity, $\sigma_{\tilde{v}}$ and C_{b2} are the constants, v is the molecular kinematic viscosity, and $S_{\tilde{v}}$ is a user-defined source term.

2.3. Droplet and Crystal Field Solution

The DROP3D solver is used in Fensap-Ice to calculate the collision of droplets and crystals on solids. In the case of two types of particles, such as droplets and ice crystals, the DROP3D solver defaults to a state of thermal equilibrium between the two particles. Therefore, both sets of dispersed phase equations are treated in an uncoupled manner [25]. The DROP3D solver calculates droplets and ice crystals in the flow field by the Eulerian method. The continuity equation and momentum equation are shown in Equations (6) and (7).

The continuity equation is as follows:

$$\frac{\partial \alpha}{\partial t} + \vec{\nabla} \cdot (\alpha \vec{V}_d) = 0 \tag{6}$$

The momentum equation is as follows:

$$\frac{\partial (\alpha \vec{V}_d)}{\partial t} + \vec{\nabla} \cdot \left[\alpha \vec{V}_d \otimes \vec{V}_d \right] = \frac{C_D Re_d}{24K} \alpha (\vec{V}_a - \vec{V}_d) + \alpha \left(1 - \frac{\rho_a}{\rho_d} \right) \frac{1}{Fr^2} \tag{7}$$

In the formula, α and $\vec{V}_d$ are the particle concentration and the mean velocity. K is the particle inertial parameter, C_D is the drag coefficient of particle, and Fr is the Froude number.

In the DROP3D solver, the calculation of droplet drag is based on the assumption that the droplets are spherical and the droplet drag model as shown in Equation (8).

$$C_D = \begin{cases} \left(\frac{24}{Re_d} \right) \left(1 + 0.15 Re_d^{0.687} \right), & Re_d \leq 1300, \\ 0.4, & Re_d > 1300. \end{cases} \tag{8}$$

The drag coefficient (C_D) of the droplet will change with the change in Reynolds number (Re_d). The droplet gradually begins to deform into a non-spherical shape when the Reynolds number exceeds 250. In calculating the drag force of ice crystals, it is also assumed that the particles are spherical and rigid, and the drag model for ice crystals as follows [25]:

$$C_d = \begin{cases} \frac{8m}{3Re_{ic}} \left[1 + \frac{mRe_{ic}}{48} + \frac{m^2}{1440} Re\, 2 \ln \left(\frac{Re_{ic}}{2} \right) \right], & Re_{ic} \leq 0.01, \\ C_{d,OB} [1 + 10^X], & 0.01 < Re_d \leq 1.5, \\ C_{d,OB} [1 + 0.138 Re_{ic}^{0.792}], & 1.5 < Re_d \leq 100, \\ C_{d,OB} [1 + 0.00087 Re_{ic}^{1.393}], & 100 < Re_d \leq 300. \end{cases} \tag{9}$$

The drag coefficients of ice crystals is derived based on an aspect ratio of 0.05; the derived drag coefficients of ice crystals are still valid when the aspect ratios are more then 0.5 [25].

2.4. Calculation of Ice Accretion Shapes

The calculation of the ice shape is implemented using the ICE3D solver in Fensap-Ice, which reads the data from DROP3D to simulate the growth of ice accumulation based on the collection efficiency of droplets and ice crystals on solid surfaces. The partial differential equations for mass conservation and energy conversion in the ICE3D solution are given in Equations (10) and (11).

The governing equation for the water film is

$$\rho_f \left[\frac{\partial h_f}{\partial t} + \vec{\nabla} \cdot (\overline{V}_f h_f) \right] = V_\infty LWC\, \beta - \dot{m}_{\text{evap}} - \dot{m}_{\text{ice}} \tag{10}$$

where ρ_f is the water film density, h_f is the water film height, $\overline{V}_f$ is the water film velocity, V_∞ is the freestream velocity, LWC is the liquid water content, β is the water droplet collection efficiency, $\dot{m}_{\text{evap}}$ is the evaporated water rate, and $\dot{m}_{\text{ice}}$ is the iced water rate.

$$\rho_f\left[\frac{\partial h_f c_f \widetilde{T}_f}{\partial t}+\vec{\nabla}\cdot\left(\overline{V}_f h_f c_f \widetilde{T}_f\right)\right]=\left[c_f\left(\widetilde{T}_\infty-\widetilde{T}_f\right)+\frac{\|\vec{V}_d\|^2}{2}\right]V_\infty LWC\,\beta$$
$$-L_{\text{evap}}\dot{m}_{\text{evap}}+\left(L_{\text{fusion}}-c_s\widetilde{T}\right)\dot{m}_{\text{ice}}+\sigma\varepsilon\left(T_\infty^4-T_{f4}\right)$$
$$-c_h\left(\widetilde{T}_f-\widetilde{T}_{\text{ice,rec}}\right)+Q_{\text{anti-icing}}. \tag{11}$$

where the first three terms on the right-hand side of the equation model the heat transfer generated by the impinging supercooled water droplets, by evaporation, and by ice accretion. The last three terms represent the radiative, convective, and 1D conductive heat fluxes. c_f is the heat capacity of the water film, the equilibrium temperature is $\widetilde{T}_f$ at the air/water film/ice/wall interface, and V_d is the droplets' impact velocity. $Q_{\text{anti-icing}}$ is the anti-icing heat flux.

Compatibility relations are needed to close the system of equations. Based on physical observations, one way to write them is as follows [25]:

$$\begin{cases} h_f \geq 0, \\ \dot{m}_{\text{ice}} \geq 0, \\ h_f\widetilde{T}_f \geq 0, \\ \dot{m}_{\text{ice}}\widetilde{T}_f \leq 0. \end{cases} \tag{12}$$

These inequalities ensure that the model predicts no liquid water in the calculations if the equilibrium temperature is below the freezing point (0 °C) and that no ice forms if the film temperature is above 0 °C.

The NTI model in FENSAP is used to analyze the collision and adhesion of ice crystals. When ice crystals impact cold surfaces, they typically rebound and move downstream, but they may partially adhere when impacting wet surfaces. The rebound and adhesion process is influenced by the normal velocity (v_n), liquid film thickness (h_f), and particle diameter (d_p). To describe this behavior, a rebound coefficient function is defined as

$$\alpha_{st}=\frac{h_f}{\max(h_f)}e^{-\chi\|v_n\|^2} \tag{13}$$

In rime-ice regions, ice crystals fully rebound ($\alpha_{st}=0$). In contrast, some ice crystals adhere to the surface in glaze-ice regions, while those in liquid-film regions fully adhere ($\alpha_{st}=1$). A critical velocity $v_c=\sqrt{\frac{2}{d_p}}$ is defined. Ice crystals partially rebound when $v_n<v_c$, whereas they fully rebound when $v_n>v_c$.

Ice crystal erosion causes angular rough protrusions on ice surfaces. The ice crystal erosion model is established based on erosion efficiency [27]:

$$\Phi_{er}=B\left(\frac{u_{t,i}}{u_0}\right)^2\left(\frac{\beta_{IWC}}{\beta_{IWC0}}\right)^{-A_1}\left(1-\frac{\eta_i}{\eta_0}\right)^{-A_2}\left(\frac{D_i}{D_0}\right)^{A_3}$$
$$\cdot\exp\left[-A_4\frac{Q_s}{R}\left(\frac{1}{T_s}-\frac{1}{T_m}\right)\right]\cdot\exp\left[-A_5\frac{Q_s}{R}\left(\frac{1}{T_i}-\frac{1}{T_m}\right)\left(1+(l_0k)^2\right)\right] \tag{14}$$

In the equation, Φ_{er} represents the ice crystal erosion efficiency; $u_{t,i}$ is the tangential velocity of ice crystal impact (m· s^{-1}); D_i is the average mass diameter of ice crystals (m); T_i is the temperature of ice crystals; κ denotes the local curvature of the ice layer; c is the chord length of the airfoil (m); T_f is the phase change temperature of ice (K); and $R=8.314$ J· mol^{-1}· K^{-1} is the ideal gas constant. The experimental constants for the ice

crystal erosion model include B at 0.58, u_0 at 84.5 m·s^{-1}, β_{IWCO} at 6 g·m^{-3}, η_0 at 0.166, D_0 at 52.7 µm, and l_0 at 0.015c, with constants A_1 to A_5 valued at 0.8, 3.0, 0.4, 3.0, and 0.1, respectively.

2.5. Establishment of the Icing Model for Blades

For wind turbine blades, the tip region experiences the most significant load variations and is also the area most prone to ice accretion. Therefore, this study focused on the tip region for numerical simulation, concentrating on simulating and analyzing the ice accretion process at the blade tip. The NACA0012 airfoil was chosen for this study, with a chord length (C) of 0.5334 m. The length and height of the flow field were set to 40C, and the leading edge of the blade was positioned 20C from the flow field boundary, as shown in Figure 2a. The inlet was defined as a velocity inlet, the outlet as a pressure outlet, and the airfoil as a no-slip. The turbulent intensity was set to the default value, and the turbulent length scale was set to 0.5334 m. Meshing was performed using ICEM with a C-type grid, and mesh refinement was applied near the airfoil region, as shown in Figure 2b.

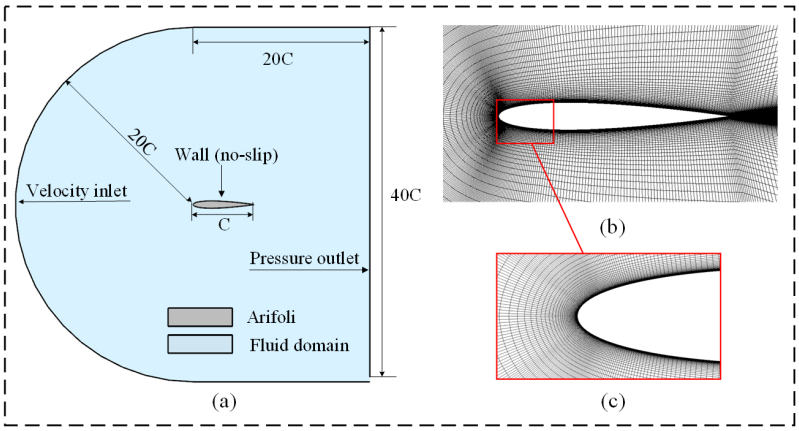

Figure 2. Computational domain: (**a**) overall domain, (**b**) blade, (**c**) clean blade leading edge.

The number of elements significantly impacts the calculation results. To accurately simulate the flow process, five different numbers of elements were used to calculate the lift coefficient, and the results are shown in Figure 3.

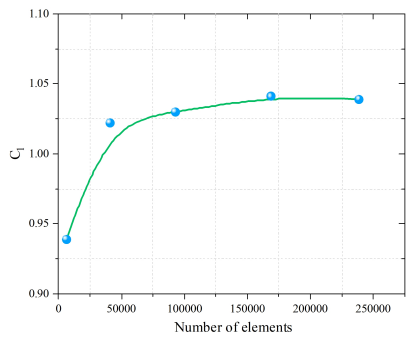

Figure 3. The lift coefficient versus the number of elements.

From Figure 3, it can be observed that the lift coefficient exhibits a converging trend as the number of elements increases, eventually reaching an asymptotic value of 1.0. When the number of elements was approximately 170,000, the mesh growth ratio was set to 1.1, achieving a mesh quality of 0.95, as shown in Figure 2b. The accuracy of the grid with approximately 170,000 mesh elements was verified using experimental data from NASA's turbulence modeling resource [28]. During the calculations, the pressure coefficient on the

blade surface was used to evaluate mesh sensitivity. The environmental parameters are presented in Table 1, and the validation results are shown in Figure 4.

As illustrated in Figure 4, the numerical simulation results exhibit a high degree of consistency with the experimental data at angles of attack of 10° and 15°. At an angle of attack of 10°, the maximum and minimum pressure coefficients align closely with the experimental data. At an angle of attack of 15°, the minimum pressure coefficient calculated using Fluent is marginally lower than the experimental data; however, the overall trend remains consistent. These findings indicate that employing an unstructured mesh after C-shaped mesh splitting ensures the accuracy of the numerical simulation results.

Table 1. Parameter settings for simulating air pressure distribution.

Description	Values
Airfoil	NACA0012
Chord length (m)	0.5334
Relative velocity (m/s)	43.8
Ambient temperature (°C)	15
Ambient pressure (pa)	101325
AoA (deg)	10°, 15°

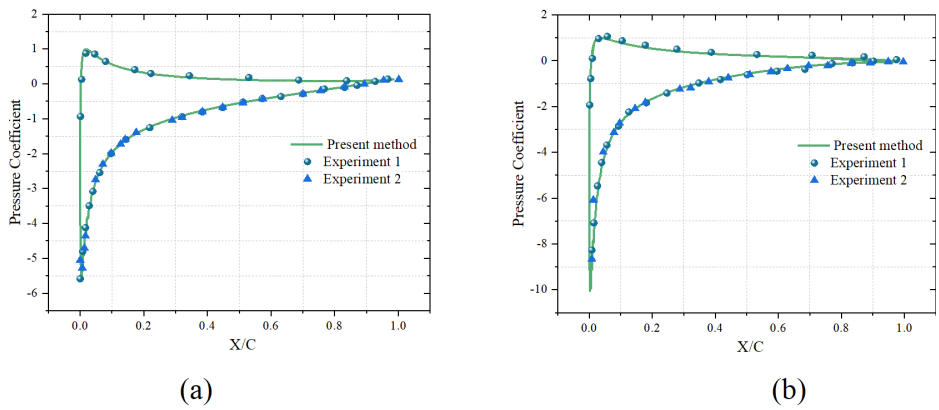

Figure 4. Validations of pressure distribution: (**a**) AoA = 10° (**b**) AoA= 15°.

3. Results and Discussion

3.1. The Role of Ice Crystals in the Icing Process

A droplet impacting a solid surface generally experiences spreading, retraction, oscillation, splash, rebound, or adhesion stages [29,30]. Finally, droplets adhering to the blade surface are driven by the airflow toward the trailing edge and form a liquid film. The film is affected by heat transfer on the blade surface and convective heat transfer with the surrounding cold air. The freezing process can be divided into five stages based on the temperature transition characteristics [31,32]: liquid cooling, nucleation, recalescence, solidification, and solid cooling. The ice crystals significantly affect the distribution of the accumulated ice on the blade surface. Therefore, ice crystals play a multifaceted role in the icing process, affecting both the droplet impact and freezing stages. Based on previous studies of supercooled droplet icing, new insights have been gained into the combined effects of ice crystals and droplets on the icing process, as shown in Figure 5.

As the ice crystals collide with the water film, droplet splashing occurs, generating secondary droplets. Additionally, the sheet-like structure of the ice crystals adheres more readily to the water film. As the adhered ice crystals accumulate, the fluidity of the water film decreases, leading to a higher concentration of the water film at the blade's leading edge. The water film releases heat through convective heat transfer and thermal conduction, which wraps around the ice crystals and causes gradual freezing, as illustrated in Figure 5b.

As the operation continues, the accumulated ice on the blade surface tends to form layered structures, increasing the ice thickness and expanding the coverage area. Furthermore, when ice crystals impact the accumulated ice on the blade surface, ice crystals continuously erode the existing ice layer, as shown in Figure 5c.

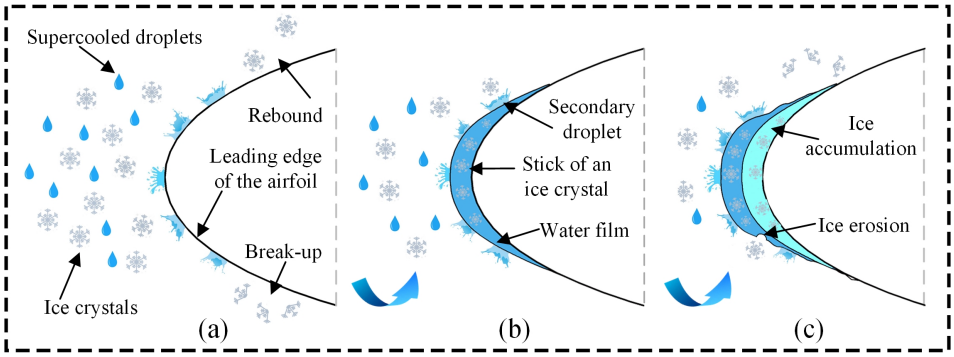

Figure 5. The blade icing process. (**a**). Droplets and ice crystals continue to impact the blade's surface. (**b**). First layer of ice accumulation. (**c**). Second layer of ice accumulation.

3.2. Icing on Static Blade

In order to ascertain the impact of ice crystals on ice shape, a series of tests were conducted in glaze ice and rime ice environments. The experimental data were sourced from collaborations with AMIL (Anti-Icing Materials International Laboratory) and CIRA (Italian Aerospace Research Center) [33]. The conditions used for validation are summarized in Table 2. Ice accretion shapes are depicted in Figure 6.

Table 2. Features of blade profile used for validation cases.

Parameter	Rime	Glaze
Relative velocity (m/s)	67.06	67.06
Ambient temperature (°C)	−7.8	−19.4
Ambient pressure (pa)	101,325	101,325
Angle of attack (deg)	4	4
MVD-droplets (μm)	20	20
LWC (g/m^3)	1	1
MVD-crystals (μm)	100	100
ICC (g/m^3)	1	1
Icing time (s)	360	360

As shown in Figure 6a, when supercooled droplets in the airflow hit the leading edge of the blade, the pressure near the leading edge is reduced due to an increase in flow velocity. Liquid water formed at the stagnation point travels toward surfaces with lower pressure and begins to form ice horns. FENSAP-ICE can accurately simulate the ice angle on the suction side, but the predicted ice shape profile is larger than the experimental measurements. The overall thickness of the blade icing is greater when droplets and ice crystals are present in the atmosphere than when only droplets are present.

In glaze ice conditions, the film water that forms after a droplet hits the surface of the blade does not freeze immediately. The ice crystals disintegrate immediately upon hitting the blade surface, resulting in a complete separation from the blade surface. However, when ice crystals collide with the water film on the airfoil surface, some adhere to the water film. These adhered ice crystals hinder the water film flow toward the trailing edge.

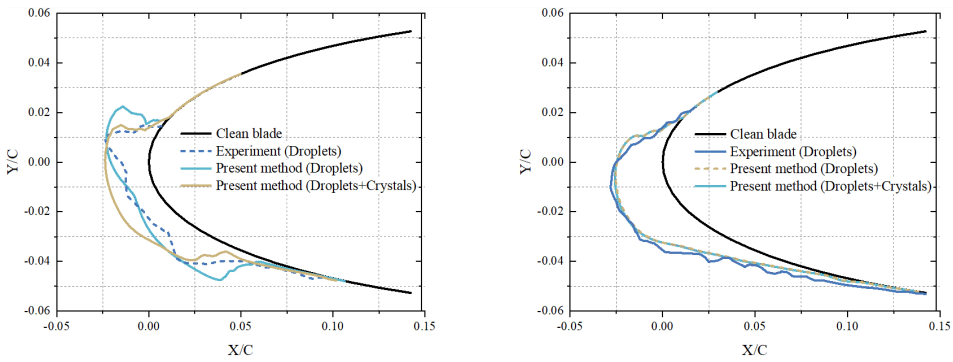

(a) (b)

Figure 6. Validations in ice shape. (**a**) Glaze ice. (**b**) Rime ice.

In rime ice conditions, FENSAP-ICE demonstrates superior predictive performance, with the predicted results exhibiting a high degree of similarity to the experimental measurements. As illustrated in Figure 6b, the ice shape formed by the droplets and ice crystals is similar to that formed when only droplets are present. This phenomenon occurs due to the low ambient temperature, which results in the immediate freezing of all the water droplets that hit the blade surface, converting them into ice. As a result, there is a lack of water film formation on the blade surface, resulting in ice crystals directly contacting the airfoil surface rather than a liquid film, which cannot influence the ice shape. In glaze ice conditions, the influence of ice crystals on the ice shape becomes more significant. Therefore, the velocity and ice thickness on the leading edge of the airfoil were analyzed. The computational results are shown in Figures 7 and 8.

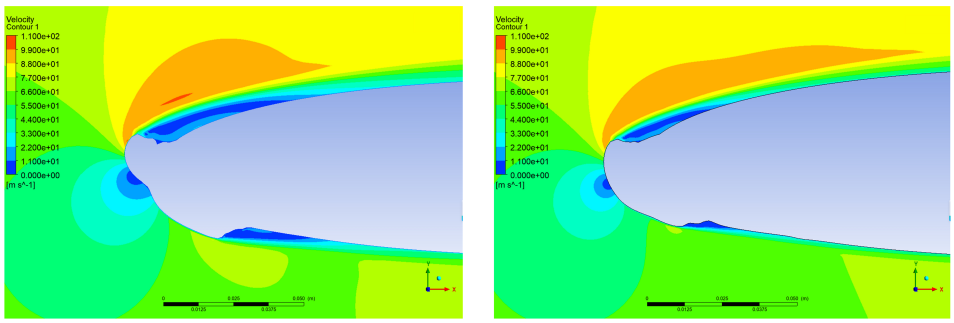

(**a**) (**b**)

Figure 7. Velocity of the leading edge of the airfoil. (**a**) Supercooled droplets. (**b**) Supercooled droplets + ice crystals.

Supercooled droplets impact the leading edge of the airfoil, causing the pressure to drop significantly. The water film spreads from the stagnation point toward the low-pressure region and gradually freezes to form ice horns on the surface. Compared to icing caused by supercooled droplets, ice crystals impacting the water film on the airfoil surface partially adhere to the water film. Ice crystals change the flow direction of the water film, significantly influencing the ice shape. In addition, a larger low-pressure region forms behind the ice horns. The low-pressure area significantly increases the residence time of supercooled droplets, promoting further freezing of the supercooled droplets and thickening the ice accumulated.

Figure 8 shows that supercooled droplet icing and ice-crystal-involved icing processes exhibit nearly constant ice growth rates. However, significant differences are observed in ice shape and thickness between the two processes. During supercooled droplet icing, the ice shape is more scattered and protruding. The maximum ice thickness at 120 s, 240 s, and 360 s is higher than in the ice-crystal-involved icing process. This results from the longer

residence time of droplets and the enhanced freezing in low-pressure regions. In contrast, ice-crystal-involved icing produces smoother and more uniform ice shapes. Ice crystals adhere to the water film upon impact, restricting its flow and limiting the growth of ice thickness. This section focuses on the effects of the median particle size of ice crystals, ice crystal concentration, ice crystal shape, and the relative concentration between ice crystals and liquid droplets on the ice shape on the blade surface.

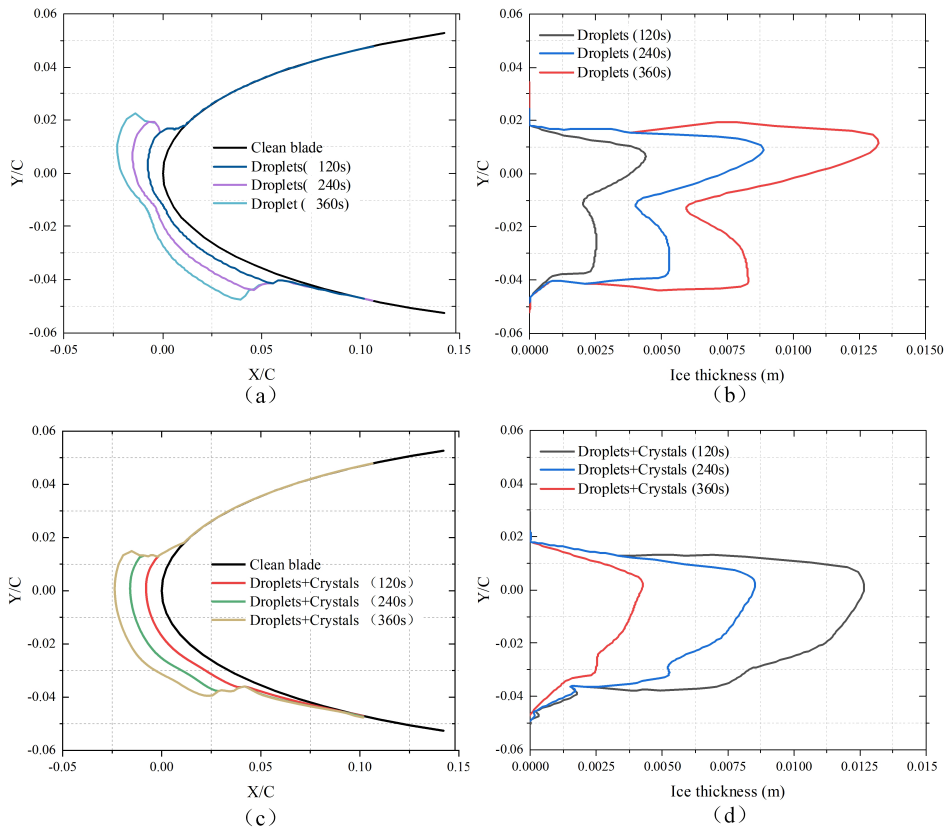

Figure 8. Ice shape and ice thickness at different times. (**a**) Ice shape (supercooled droplets). (**b**) Ice thickness (supercooled droplets). (**c**) Ice shape (supercooled droplets + ice crystals). (**d**) Ice thickness (supercooled droplets + ice crystals).

3.3. The Influence of MVD-Crystals

As the size of the ice crystals changes, the fluidity of the liquid film on the blade surface also changes accordingly, affecting the entire ice accretion process. For this purpose, four different ice crystal sizes (50, 100, 150, and 200 μm) were selected to experimentally simulate ice accretion. In these experiments, the critical role of particle size variation in the ice accretion process was revealed by a detailed analysis of how ice crystals of different sizes affect the mobility of the liquid film and the ice shapes on the blade surface. To ensure the reliability of the experimental results, other variables were strictly controlled, ensuring that the observed changes in ice shape accurately reflect the effect of ice crystal particle size on the ice shape. The simulation parameters are shown in Table 3, while the ice shape on the blade surface at different particle sizes is shown in Figure 9.

As shown in Figure 9, the median particle size of the ice crystals not only altered the thickness of the accumulated ice but also affected the distribution of the ice on the blade surface. Smaller ice crystals are more likely to be carried toward the trailing edge of the blade by airflow and the liquid film after impacting the blade surface. As a result, thinner ice accumulates in the leading-edge region. The ice shape is similar to that observed when only droplets are present. However, as the ice crystal particle size increases, larger ice crystals are less influenced by airflow after impact and have a greater contact area with

the liquid film. Consequently, more ice crystals adhere to the leading edge of the blade. Therefore, ice crystal particle size changes directly affect the ice shape at the leading edge, further intensifying ice accumulation in that region.

Table 3. Ice shape simulation parameter settings under different relative velocities.

Parameter	Value
Relative velocity (m/s)	67.06
Ambient temperature (°C)	−7.8
Ambient pressure (Pa)	101,325
AoA (deg)	4
MVD-droplets (μm)	20
LWC (g/m^3)	1
MVD-crystals (μm)	100
ICC (g/m^3)	0.5
Icing time (s)	360

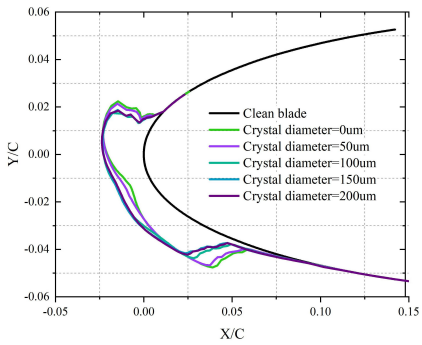

Figure 9. Ice shape under different MVD-crystals.

3.4. The Influence of Crystal Aspect Ratio

The aspect ratio of ice crystals significantly influences their adhesion to the liquid film, thereby altering the ice shape on the blade surface. To further investigate the effect of different ice crystal aspect ratios on the ice accretion process, numerical simulation experiments were conducted with ice crystals having aspect ratios of 0.05, 0.1, 0.4, and 1. The specific simulation parameters are detailed in Table 3, and the ice shapes for each aspect ratio are shown in Figure 10.

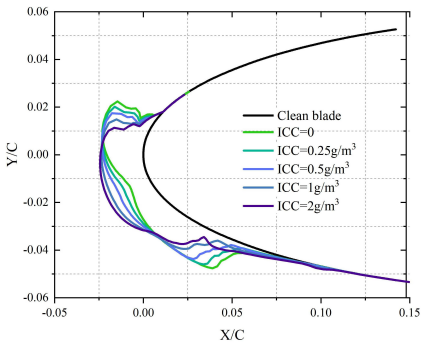

Figure 10. Ice shape under different crystal aspect ratios.

As shown in Figure 10, changes in the shape of ice crystals not only affect their collision behavior but also significantly influence the formation and distribution of the ice shape. When the aspect ratio was 0.05, the ice crystals were elongated, making them more prone to move with the airflow. This reduced the attachment area on the blade surface and caused the accumulated ice to be more dispersed. As the aspect ratio increased, the ice crystals

became more flattened, improving their ability to adhere to the liquid film on the blade surface and impeding the flow of the liquid film. Subsequently, the liquid film, encasing the ice crystals, gradually froze at the leading edge, forming a more uniform ice layer. The results indicate that the aspect ratio of ice crystals has a significant impact on the ice shape. Flattened ice crystals lead to a thicker ice layer, which directly influences the distribution of ice crystals on the blade surface and the overall ice shape.

3.5. The Influence of Ice Crystal Concentration

The concentration of ice crystals not only directly affects the frequency of ice crystal impacts on the blade surface but also influences the distribution of ice crystals around the blade, thereby altering the ice shape. To further investigate the influence of ice crystal concentration on the ice shape, simulations were conducted with four different ice crystal concentrations (0.25, 0.5, 1, and 2 g/m^3). The ice shapes formed under these different concentrations were analyzed through simulations. The relevant experimental parameters are shown in Table 3, and the simulation results for ice shapes under different ice crystal concentrations are shown in Figure 11.

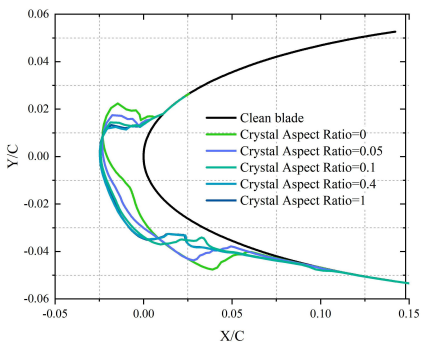

Figure 11. Ice shapes under different ice crystal concentrations.

As shown in Figure 11, the attachment rate of ice crystals to the leading edge of the blade increased significantly with rising ice crystal concentration, leading to marked changes in both ice shape and ice thickness. At an ice crystal concentration of 2 g/m^3, the ice thickness on the blade surface reached its maximum. At lower concentrations, the ice spread continuously toward both sides of the leading edge, resulting in an ice shape similar to that formed in the presence of only liquid droplets. However, as the ice crystal concentration continued to increase, the aggregation of ice crystals in the leading-edge region became more pronounced. Ice crystals adhered more to the liquid film, causing a reduction in ice on both sides of the leading edge and a significant increase in ice thickness in the central region of the leading edge.

3.6. Aerodynamic Analysis of Iced Blades

Ice-covered blades not only increase the surface roughness but also disturb the streamlines of airflow around the blades, significantly affecting the aerodynamic performance of wind turbine units. Additionally, changes in the AoA can substantially impact the aerodynamic characteristics of wind turbine units. To assess the effect of the overlying ice shape on aerodynamic performance under varying AoAs and the combined influence of ice crystals and liquid droplets, numerical simulations were conducted. The streamlines around clean blades and two types of ice-covered blades, as well as the ice shapes of these covered blades, were calculated for different AoAs. The AoA was set to 5°, 10°, 15°, and 20° during the numerical simulations. Streamlines were generated using TECPLOT after importing data from FLUENT. The parameter settings are provided in Table 4, and the streamlines for different AoAs are illustrated in Figure 12.

Table 4. Icing conditions.

Parameters	Values
Relative velocity (m/s)	67.06
Ambient temperature (°C)	−7.8
Ambient pressure (Pa)	101,325
AoA (deg)	5°, 10°, 15°, 20°
MVD-droplets (μm)	20
LWC (g/m^3)	0.5
MVD-crystals (μm)	100
ICC (g/m^3)	0.5
Icing time (s)	600

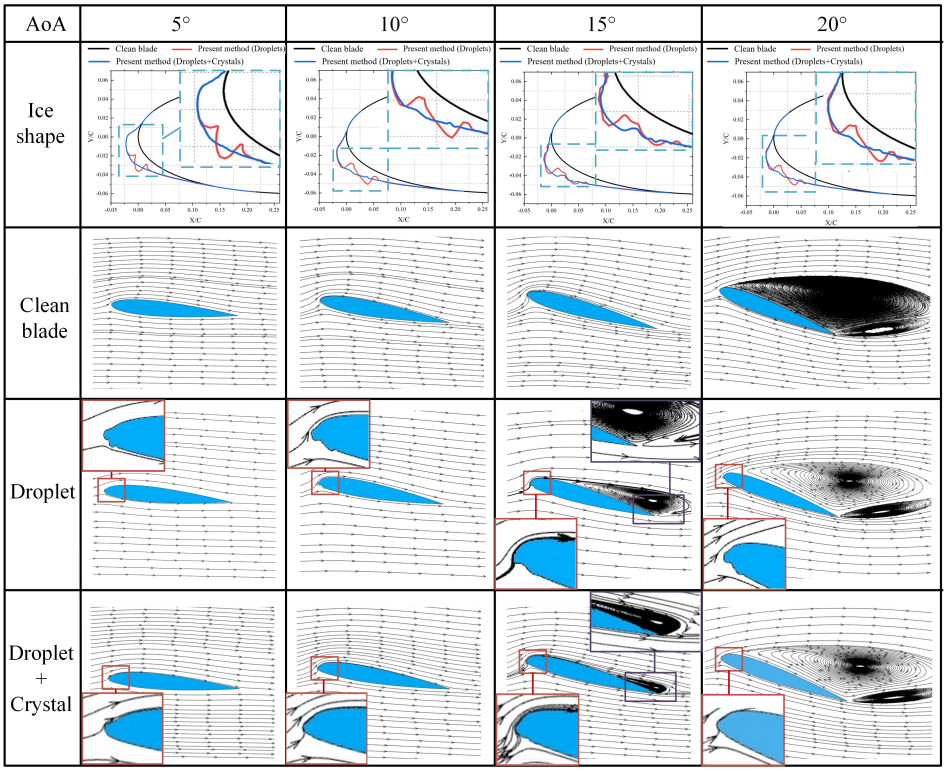

Figure 12. Ice accretion features after 10 min.

As shown in Figure 12, when the AoA ranged from 5° to 20°, the ice shape caused by the liquid droplets exhibited distinct ice corners. As the AoA increased, the ice corner on the pressure side gradually shifted toward the trailing edge of the blade. However, when ice crystals interacted with the droplets, the ice shape changed significantly; the ice corners disappeared, resulting in a smoother and fuller ice shape.

When the AoA of the clean blade was less than 20°, increasing the AoA did not significantly disturb the flow field around the airfoil, and the streamlines remained quite regular. At an AoA of 20°, however, separation vortices appeared on the suction side of the clean blade, indicating airflow separation from the blade surface. This resulted in a stall, causing a decrease in lift and an increase in drag. At an AoA of 15°, separation vortices formed at the trailing edge of the airfoil under both ice accretion conditions. Compared to the ice shape formed under the combined effect of ice crystals and droplets, the ice shape caused by droplets alone produced a larger separation vortex near the trailing edge. Therefore, the ice-covered blade has a greater impact on aerodynamic performance at an

AoA of 15° under the action of liquid droplets alone than under the combined action of ice crystals and liquid droplets.

As the AoA increased to 20°, the separation vortex on the suction side moved forward, and its area of influence expanded. A small secondary vortex appeared behind the primary separation vortex for both clean and ice-covered blades. In summary, as the AoA increased, the flow around the airfoil became increasingly turbulent. When the AoA exceeded the stall angle, separation vortices and secondary vortices formed at the trailing edge, significantly increasing airflow disturbances and severely degrading the aerodynamic performance of the blades.

Figure 13 illustrates the relationship between lift and drag coefficients and angle of attack (AoA) for clean blades and two types of iced blades. Within the range of 0°–10° of the angle of attack (AoA), the increases in lift and drag coefficients are not significantly pronounced, with both clean and iced blade profiles displaying a consistent trend in drag coefficient variation. As the AoA continues to increase beyond 10°, stall onset is characterized by a sudden drop in lift coefficient and a significant rise in drag coefficient. The presence of ice horns on the blade surface leads to increased surface roughness, which accelerates the onset of stall. Consequently, for AoA values exceeding 10°, the drag coefficient experiences a sharp increase as atmospheric droplets form ice accretions on the blade surface. However, when both atmospheric droplets and ice crystals coexist, the stall angle is delayed to approximately 15°, indicating a modification in aerodynamic behavior.

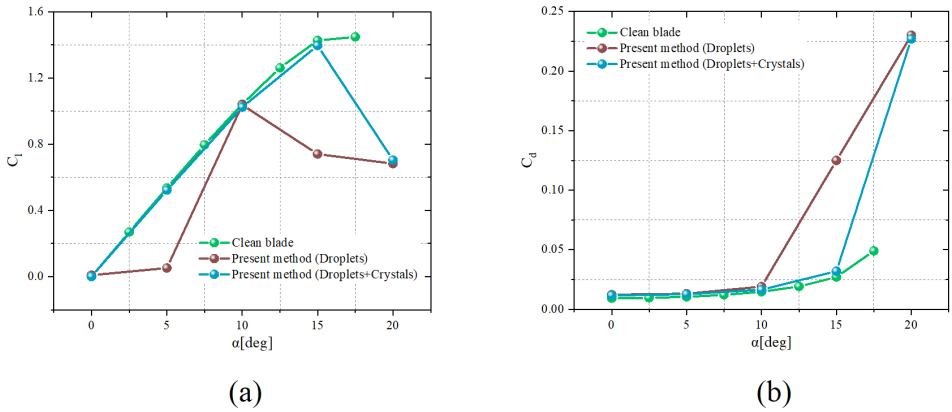

(a) (b)

Figure 13. Lift coefficients and drag coefficients. (**a**) Lift coefficients. (**b**) Drag coefficients.

The lift-to-drag ratio Cl/Cd is a critical indicator of wind turbine performance, providing insight into the aerodynamic efficiency of turbine blades. An increase in Cl/Cd indicates enhanced lift generation relative to drag, thereby improving energy extraction from the wind. To evaluate the impact of icing on the Cl/Cd ratio, clean blades and blades with droplet-induced icing were used as control conditions. This study specifically investigates the effects of mixed icing conditions, involving both ice crystals and droplets, on the Cl/Cd ratio. The Cl/Cd ratios for all three blade conditions are illustrated in Figure 14.

Figure 14 demonstrates that at an angle of attack (AoA) of 10°, the Cl/Cd ratio for both the clean and ice-covered blades attains its peak value. For blades covered with ice formed solely from atmospheric droplets, the Cl/Cd ratio decreases by 22.9% compared to the clean blade. A stall phenomenon occurs at an AoA of 10°, resulting in increased aerodynamic drag. The ice shape formed by droplets causes the Cl/Cd ratio to decrease from 54.578 to 5.98, a reduction of 89%. For ice-covered blades caused by both droplets and ice crystals, the Cl/Cd ratio is reduced by 12.37%. As the AoA increases from 15° to 20°, the Cl/Cd ratio drops sharply from 43.6 to 3.1, marking a 93% reduction.

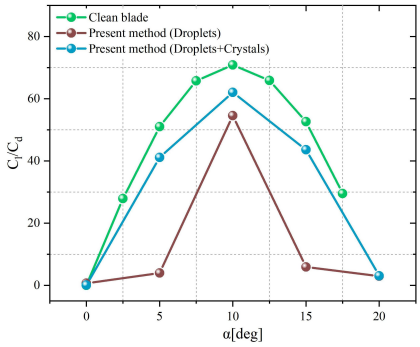

Figure 14. Comparison of *Cl*/*Cd* for the clean and iced blades.

4. Conclusions

This study employed the FENSAP-ICE simulation tool to investigate the ice accretion process involving ice crystals and supercooled liquid droplets under clear ice conditions. The effects of different ice crystal parameters on ice shape and mass were analyzed, as were the impact of AOA and icing time on the aerodynamic performance of the blades.

The results show that the ice shape formed by the combined action of ice crystals and supercooled droplets differs significantly from the ice shape generated solely by droplets. Under the action of droplets alone, the resulting ice shape is characterized by pronounced ice corners and high surface roughness. In contrast, the ice shape formed by the combined effect of ice crystals and supercooled droplets is smoother and fuller. Moreover, as ice crystal concentration and particle size increase, the ice thickness increases significantly, while the prominence of ice corners diminishes.

As the AoA increases, clean blades exhibit highly regular streamlines at 15°, whereas the two ice-covered blades form separation vortices near the airfoil tip. The area of the separation vortex generated by droplets alone is larger than that formed by the combined action of droplets and ice crystals. This suggests that at 15°, the ice shape resulting from droplet-induced icing has a more significant impact on the blade's aerodynamic performance.

The aerodynamic analysis indicates that as the airfoil's AoA increases from 0° to 10°, the lift and drag coefficients of both iced and clean airfoils keep the same values. For AoA values exceeding 10°, the lift coefficient decreases while the drag coefficient increases, indicating a divergence in aerodynamic characteristics attributable to the effects of icing. Such fluctuations in aerodynamic performance directly influence the wind turbine's energy capture efficiency and stable operation.

In summary, this study reveals the critical role of ice crystals in the blade icing process and elucidates the icing mechanism under complex meteorological conditions. These findings provide a scientific foundation for developing efficient anti-icing and de-icing technologies.

Author Contributions: B.Y.: methodology, software, validation, formal analysis, writing—original draft preparation. A.J.: conceptualization, investigation, supervision, funding acquisition, writing—review and editing. J.C.: methodology, funding acquisition. S.Z.: software, formal analysis. B.J.: validation. All authors have read and agreed to the published version of the manuscript.

Funding: The work reported above was supported by the National Key Research and Development Program of China (2021YFB1506902), Natural Science Foundation of China (12362033), Xinjiang Uygur Autonomous Region 'Two Regions' Science and Technology Development Programme of China (2023LQ01001), and Xinjiang University Outstanding Doctoral Student Innovation Project of China (XJU2024BS105).

Institutional Review Board Statement: Not applicable.

Informed Consent Statement: Not applicable.

Data Availability Statement: The original contributions presented in this study are included in the article. Further inquiries can be directed to the corresponding author.

Conflicts of Interest: Author Bang Jiang were employed by Zhu Zhou Times New Material Technology Co., Ltd. The remaining authors declare that the research was conducted in the absence of any commercial or financial relationships that could be construed as a potential conflict of interest.

References

1. Dai, Y.; Xie, F.; Li, B.; Wang, C.; Shi, K. Effect of blade tips ice on vibration performance of wind turbines. *Energy Rep.* **2023**, *9*, 421–433. [CrossRef]
2. Douvi, E.; Douvi, D. Aerodynamic characteristics of wind turbines operating under hazardous environmental conditions: A review. *Energies* **2023**, *16*, 7681. [CrossRef]
3. Ibrahim, G.M.; Pope, K.; Naterer, G.F. Extended scaling approach for droplet flow and glaze ice accretion on a rotating wind turbine blade. *J. Wind Eng. Ind. Aerodyn.* **2023**, *233*, 105296. [CrossRef]
4. Wang, Q.; Yi, X.; Liu, Y.; Ren, J.; Yang, J.; Chen, N. Numerical investigation of dynamic icing of wind turbine blades under wind shear conditions. *Renew. Energy* **2024**, *227*, 120495. [CrossRef]
5. Virk, M.S.; Homola, M.C.; Nicklasson, P.J.; Sundsbø, P.A. Effect of rime ice accretion on aerodynamic characteristics of wind turbine blade profiles. *Wind Eng.* **2010**, *34*, 207–218. [CrossRef]
6. Pouryoussefi, S.G.; Mirzaei, M.; Nazemi, M.M. Experimental study of ice accretion effects on aerodynamic performance of NACA-23012 airfoil. *Chin. J. Aeronaut.* **2016**, *29*, 585–595. [CrossRef]
7. Merizalde, Y.; Hernández-Callejo, L.; Duque-Perez, O.; Alonso-Gómez, V. Maintenance models applied to wind turbines: A comprehensive overview. *Energies* **2019**, *12*, 225. [CrossRef]
8. Li, X.; Chi, H.; Li, Y.; Xu, Z.; Guo, W.; Feng, F. An experimental study on blade surface de-icing characteristics for wind turbines in rime ice condition by electro-thermal heating. *Coatings* **2024**, *14*, 94. [CrossRef]
9. Manatbayev, R.; Baizhuma, Z.; Bolegenova, S.; Georgiev, A. Numerical simulations on static vertical axis wind turbine blade icing. *Renew. Energy* **2021**, *170*, 997–1007. [CrossRef]
10. Rekuviene, R.; Saeidiharzand, S.; Mažeika, L.; Samaitis, V.; Jankauskas, A.; Sadaghiani, A.K.; Gharib, G.; Muganlı, Z.; Koşar, A. A review on passive and active anti-icing and de-icing technologies. *Appl. Therm. Eng.* **2024**, *250*, 123474. [CrossRef]
11. He, Z.; Xie, H.; Jamil, M.I.; Li, T.; Zhang, Q. Electro-/photo-thermal promoted anti-icing materials: A new strategy combined with passive anti-icing and active de-icing. *Adv. Mater. Interfaces* **2022**, *9*, 2200275. [CrossRef]
12. Homola, M.C.; Virk, M.S.; Nicklasson, P.J.; Sundsbø, P.A. Performance losses due to ice accretion for a 5 MW wind turbine. *Wind Energy* **2012**, *15*, 379–389. [CrossRef]
13. Wang, Z.; Zhu, C. Numerical simulation of three-dimensional rotor icing in hovering flight. *Proc. Inst. Mech. Eng. Part G J. Aerosp. Eng.* **2018**, *232*, 545–555. [CrossRef]
14. Timmer, W.A.; van Rooij, R.P.J.O.M. Summary of the Delft University wind turbine dedicated airfoils. *J. Sol. Energy Eng.* **2003**, *125*, 488–496. [CrossRef]
15. Yirtici, O.; Cengiz, K.; Ozgen, S.; Tuncer, I.H. Aerodynamic validation studies on the performance analysis of iced wind turbine blades. *Comput. Fluids* **2019**, *192*, 104271. [CrossRef]
16. Gao, L.; Liu, Y.; Zhou, W.; Hu, H. An experimental study on the aerodynamic performance degradation of a wind turbine blade model induced by ice accretion process. *Renew. Energy* **2018**, *133*, 663–675. [CrossRef]
17. Guan, X.; Li, M.; Wu, W.; Xie, Y.; Sun, Y. Research on formation mechanism and output effect of wind turbine ice-covered blades. *Wind Eng.* **2024**, *48*, 345–358. [CrossRef]
18. Sokolov, P.; Jin, J.Y.; Virk, M.S. Accreted ice mass ratio (k-factor) for rotating wind turbine blade profile and circular cylinder. *Wind Energy* **2019**, *22*, 447–457. [CrossRef]
19. Wang, C.; Lin, W.; Lin, X.; Wu, T.; Meng, Z.; Cai, A.; Xu, Z.; Li, Y.; Feng, F. The Influence of Angle of Attack on the Icing Distribution Characteristics of DU97 Blade Airfoil Surface for Wind Turbines. *Coatings* **2024**, *14*, 160. [CrossRef]
20. Liang, D.; Zhao, P.; Shen, H.; Yang, S.; Chi, H.; Li, Y.; Feng, F. An Experimental Study of Surface Icing Characteristics on Blade Airfoil for Offshore Wind Turbines: Effects of Chord Length and Angle of Attack. *Coatings* **2024**, *14*, 623. [CrossRef]
21. Han, Y.; Lei, Z.; Dong, Y.; Wang, Q.; Li, H.; Feng, F. The Icing Characteristics of a 1.5 MW Wind Turbine Blade and Its Influence on the Blade Mechanical Properties. *Coatings* **2024**, *14*, 242. [CrossRef]
22. Hu, Y.; Pan, J.; Liu, Y.; Zhang, C.; Jiang, Y.; Zhu, J. Research on icing model and calculation methods. *Phys. Fluids* **2024**, *36*, 093334. [CrossRef]
23. Xu, Z.; Zhang, T.; Li, X.; Li, Y. Effects of ambient temperature and wind speed on icing characteristics and anti-icing energy demand of a blade airfoil for wind turbine. *Renew. Energy* **2023**, *217*, 119135. [CrossRef]

24. Chen, J.; Zhang, Y.; Fu, S. Roughness implementation and convective heat transfer coefficient computation toward ice accretion simulation. *Phys. Fluids* **2023**, *35*, 114102. [CrossRef]
25. ANSYS Inc. *ANSYS FENSAP-ICE User Manual*; ANSYS Inc.: Canonsburg, PA, USA, 2017.
26. Shukla, V.; Kaviti, A.K. Performance evaluation of profile modifications on straight-bladed vertical axis wind turbine by energy and Spalart Allmaras models. *Energy* **2017**, *126*, 766–795. [CrossRef]
27. Trontin, P.; Blanchard, G.; Villedieu, P. A Comprehensive numerical model for mixed-phase and glaciated icing conditions. In Proceedings of the 8th AIAA Atmospheric and Space Environments Conference, Washington, DC, USA, 13–17 June 2016; Paper No. 3742; AIAA: Reston, VA, USA, 2016.
28. Gregory, N.; O'Reilly, C.L. Low-speed aerodynamic characteristics of NACA 0012 aerofoil section, including the effects of upper-surface roughness simulating hoar frost. *Aeronaut. Res. Counc. Rep. Mem.* **1970**, *3726*, 1–33.
29. Zhong, Y.; Lin, H.; Jin, Z.; Yang, Z. The impact, freezing, and melting processes of a supercooled water droplet onto a cold slippery liquid-infused porous surface. *Int. J. Heat Mass Transf.* **2024**, *224*, 125306. [CrossRef]
30. Yang, X.; Wang, K.; Liu, J.; Kang, P.; Liu, X. Experimental study on freezing characteristics of droplet impact on cold cylindrical surfaces. *Int. Commun. Heat Mass Transf.* **2024**, *157*, 107769. [CrossRef]
31. Meng, Z.; Zhang, P. Dynamic propagation of ice-water phase front in a supercooled water droplet. *Int. J. Heat Mass Transf.* **2020**, *152*, 119468. [CrossRef]
32. Akhtar, S.; Xu, M.; Mohit, M. A comprehensive review of modeling water solidification for droplet freezing applications. *Renew. Sustain. Energy Rev.* **2023**, *188*, 113768. [CrossRef]
33. Fortin, G.; Ilinca, A.; Laforte, J.L. Prediction of 2D airfoil ice accretion by bisection method and by rivulets and beads modeling. In Proceedings of the 41st Aerospace Sciences Meeting and Exhibit, Reno, NV, USA, 6–9 January 2003; Paper No. 1076.

Disclaimer/Publisher's Note: The statements, opinions and data contained in all publications are solely those of the individual author(s) and contributor(s) and not of MDPI and/or the editor(s). MDPI and/or the editor(s) disclaim responsibility for any injury to people or property resulting from any ideas, methods, instructions or products referred to in the content.